Asian Journal of Chemistry; Vol. 38, No. 1 (2026), 45-54
ASIAN JOURNAL OF CHEMISTRY
https://doi.org/10.14233/ajchem.2026.34785

Tailoring of Copper(II) Oxide-Cellulose Nanocomposites for Efficient Photocatalytic Degradation of Thymol Blue

HAFEEZUR REHMAAN[1], JASPAL SINGH[1,*], PAYAL DEVI[1], NAWAL KISHOR[1], NITISH KUMAR[2], PAYAL SHARMA[1] and ANJALI[1]

[1]Department of Chemistry, Gurukula Kangri (Deemed to be University), Haridwar-249404, India
[2]Graduate Institute of Biomedical Engineering, National Chung Hsing University, Taichung, Taiwan

*Corresponding author: E-mail: sjs2874@yahoo.com

Received: 28 August 2025 *Accepted*: 28 October 2025 *Published online*: 31 December 2025 AJC-22220

The widespread release of synthetic dyes into aquatic ecosystems poses a serious environmental risk as a result of their toxicity, persistence and resistance to biodegradation. In this study, cellulose extracted from banana peels was combined with synthesized copper(II) oxide nanoparticles to fabricate CuO-cellulose nanocomposites for visible-light-driven degradation of thymol blue (ThB). The cellulose was isolated through sequential alkaline treatment, bleaching and acid hydrolysis, while CuO nanoparticles were prepared *via* co-precipitation and subsequent calcination. The nanocomposites were obtained by refluxing CuO with dispersed cellulose under alkaline conditions. Structural and compositional analyses through XRD, FTIR, XPS and FE-SEM/EDX confirmed the monoclinic CuO phase, the preservation of cellulose crystallinity and uniform nanoparticle anchoring on the cellulose matrix. UV-Vis DRS and Tauc analysis revealed that incorporation of cellulose effectively narrowed the band gap of CuO, enhancing visible-light absorption and interfacial charge transfer. Photocatalytic performance was assessed using ThB dye under controlled pH and temperature. Among the investigated compositions, the CuO-cellulose (3%) nanocomposite at 0.20 g/L exhibited the highest degradation efficiency, attributed to improved adsorption capacity, suppressed charge recombination and enhanced ROS generation. The results demonstrate the synergistic interaction between CuO and cellulose, offering a low-cost, sustainable and efficient photocatalyst for the removal of organic pollutant under visible light.

Keywords: Photocatalysis, Thymol blue, Wastewater treatment, Organic pollutants, Copper(II) oxide, Cellulose.

INTRODUCTION

Among the most urgent issues the world now faces are the environmental consequences of agricultural activities, water contamination and the regulation of seaweed cultivation in medical plant irrigation [1-4]. Industrial effluents damaged freshwater sources significantly, hence endangering environmental integrity as well as human health [5]. Among such contaminants, synthetic organic dyes often employed in sectors including textiles, plastics, printing and food processing are of special concern given their toxicity, stability and low biodegradability [6-8]. The indiscriminate release of dyes is a momentous contributor to water contamination [9-12] and removing these dyes efficiently plays a significant role in enhancing water quality and survival of aquatic species [13,14]. The traditional ways to remove dyes include biological treatment, coagulation, flocculation, absorption, membrane filtering and electrochemical and advanced oxidation processes (AOPs) [15-21]. Among all these, AOPs are the most promising due to their simplicity, low cost, operational feasibility and their ability to minimize organic contaminants effectively [8,22-25]. These procedures require modification by the incorporation of metal oxide-cellulose nanocomposite for the effective exclusion of organic pollutants from wastewater [26].

Copper(II) oxide possesses a narrow energy band gap in the range of 1.2-2.6 eV, which makes it highly efficient for various applications. It is a p-type semiconducting material [27] with excellent stability under visible light, high thermal resistance and good biocompatibility [28-30]. These properties render CuO particularly effective for sensing, environmental remediation and energy storage applications [31-33]. Literature survey suggests that copper(II) oxide nanoparticles have wide applications in photocatalysis, gas sensing, solar cells and lithium-ion batteries [34-36]. The incorporation of cellulose with metal oxide nanomaterials significantly enhances the performance as effective adsorbents for wastewater treat-

ment [37,38]. Owing to its biodegradable and renewable nature, semi-crystalline structure, high tensile strength and tunable surface chemistry, cellulose provides an excellent supporting matrix for metal-based nanocomposites [39]. In particular, cellulose nanocrystals (CNCs), with dimensions in the range of 45-65 nm, offer an exceptionally high surface area and remarkable water retention capacity, which greatly promote pollutant adsorption [40]. These attributes make metallic-based cellulose nanocomposites highly promising, low-cost, and sustainable materials for the efficient removal of organic contaminants from wastewater.

Recent studies on various types of nanocomposites have demonstrated their excellent adsorption and photocatalytic degradation efficiencies toward dyes such as methylene blue (MB) and thymol blue (ThB). Nanocomposites based on graphene oxide, Fe_3O_4 and ZnO-Al_2O_3 have also shown significant removal of both ThB and MB dyes [41,42]. In addition, cost-effective copper(II) oxide nanoparticles, known for their low toxicity and high chemical reactivity, have proven to be highly efficient photocatalysts for the degradation of methylene blue [43-45]. In this work, copper(II) oxide-cellulose nanocomposites were synthesized using a co-precipitation method combined with a high-temperature reflux process. Comprehensive characterization was carried out to evaluate the physicochemical properties of the nanocomposites, including crystallinity, structure, morphology, optical behaviour and elemental states. The photocatalytic removal of thymol blue dye under visible-light irradiation was investigated using nanocomposites with different molecular topologies.

EXPERIMENTAL

All chemicals and solvents (LR grade) were used without further purification. Copper(II) acetate monohydrate was procured from Sigma-Aldrich, Germany. Thymol blue (ThB) dye, sodium hydroxide, hydrochloric acid and hydrogen peroxide (30% v/v) were obtained from Central Drug House (CDH), Mumbai, India.

Extraction of cellulose (CNC) from banana peel: Banana peels sourced from a grocery, were chopped and treated with warm water washing to remove contaminants. The material was air-dried for 3 days to obtain a powder, which was then treated with alkali to remove waxes, oils, lignin and hemicellulose, followed by washing with distilled water to eliminate residual alkali. Acid hydrolysis of the biomass was subsequently performed under controlled temperature and time conditions. The hydrolyzed material was then stirred with distilled water, filtered, bleached and dried. This pre-treated biomass was used for further nanocomposite preparation

Synthesis of copper(II) oxide nanoparticles: The co-precipitation method was used to fabricate copper(II) oxide nanocomposite [46]. Briefly, a 0.5 M NaOH solution was added dropwise to a 0.5 M aqueous solution of copper(II) acetate monohydrate, adjusting the pH to 11. The mixture was stirred for several hours until a black precipitate formed. The precipitate was then centrifuged at 5000 rpm for 5 min, washed with ethanol and distilled water, and dried in an oven at 60 ºC. The dried material was ground and subsequently calcined at 250 ºC for 2 h to obtain copper(II) oxide nanoparticles.

Fabrication of copper(II) oxide-cellulose nanocomposites: The nanocomposite was prepared using a refluxing method [47]. A 100 mL aqueous dispersion of copper(II) oxide nanoparticles was prepared and stirred continuously. The dispersed cellulose solution in varied composition (1%, 3%, 5% and 10%) was then added gradually and the mixture was stirred for 2 h, followed by the addition of 0.2 M NaOH solution dropwise to maintain the pH at 11. The reaction mixture was refluxed at 110 ºC for 2 h, resulting in the formation of a black copper(II) oxide-cellulose nanocomposites.

Characterization: The characterization of synthesized copper(II) oxide-cellulose nanocomposites was performed using XRD (Advanced Bruker D-8) with Cu*K*α radiation (λ = 1.54 Å) at 40 kV. Crystalline planes, phase purity and structural features were examined over a 2θ range of 5º-90º. Functional groups and metal-oxide linkages were analyzed using FT-IR (Shimadzu 8400-S) in the range of 4000-400 cm^{-1}. Surface morphology and elemental composition were determined using FE-SEM equipped with EDX (Apreo S), along with XPS analysis. The optical properties of the nanocomposites were evaluated using diffuse reflectance spectroscopy and a UV–Vis spectrophotometer

Photocatalytic assessment of thymol blue (ThB): Thymol blue (ThB) was used as a model dye to evaluate the photocatalytic degradation efficiency of the copper(II) oxide-cellulose nanocomposites. Photocatalytic experiments were conducted in a 400 mL borosilicate glass reactor under visible-light irradiation. A 20 ppm ThB solution was prepared for the study. For adsorption-desorption equilibrium, 50 mL of ThB solution was mixed with 0.20 g/L of each nanocomposite catalyst and stirred in the dark for 120 min. The residual concentration of ThB dye was monitored using a UV-Vis spectrophotometer (Shimadzu 2450).

The photocatalytic degradation experiments were then carried out under visible light with nanocomposites of different concentrations. At regular intervals, 1.5 mL of reaction mixture was withdrawn, centrifuged at 5000 rpm (Eltek TC 450 D), and analyzed. The absorbance of ThB dye at 434 nm was recorded to determine the degradation rate. A control experiment without catalyst was also performed under identical conditions. Throughout all experiments, the solution temperature and pH were maintained at 28 ºC and 7, respectively, to ensure consistent reaction conditions.

RESULTS AND DISCUSSION

XRD analysis: Fig. 1a displays the X-ray diffraction patterns of pure CuONPs and cellulose samples. The CuONPs sample exhibits several sharp and well-defined peaks at 2θ values indicating its crystalline nature. The 2θ peaks at 31.88º, 35.50º, 36.10º, 38.80º, 44.30º, 48.70º, 51.44º and 61.72º, corresponding to the (110), $(\bar{1}11)$, (111), $(\bar{2}02)$, (202), (020), $(\bar{1}13)$ and (113) crystal planes, respectively. These peaks correspond to the monoclinic phase of CuO, consistent with the JCPDS card no. 00-048-1548 [48]. On the other hand, the cellulose sample shows a broad peak around 22º, characteristic of its semi-crystalline structure. This broadening reflects the typical amorphous regions within the cellulose matrix

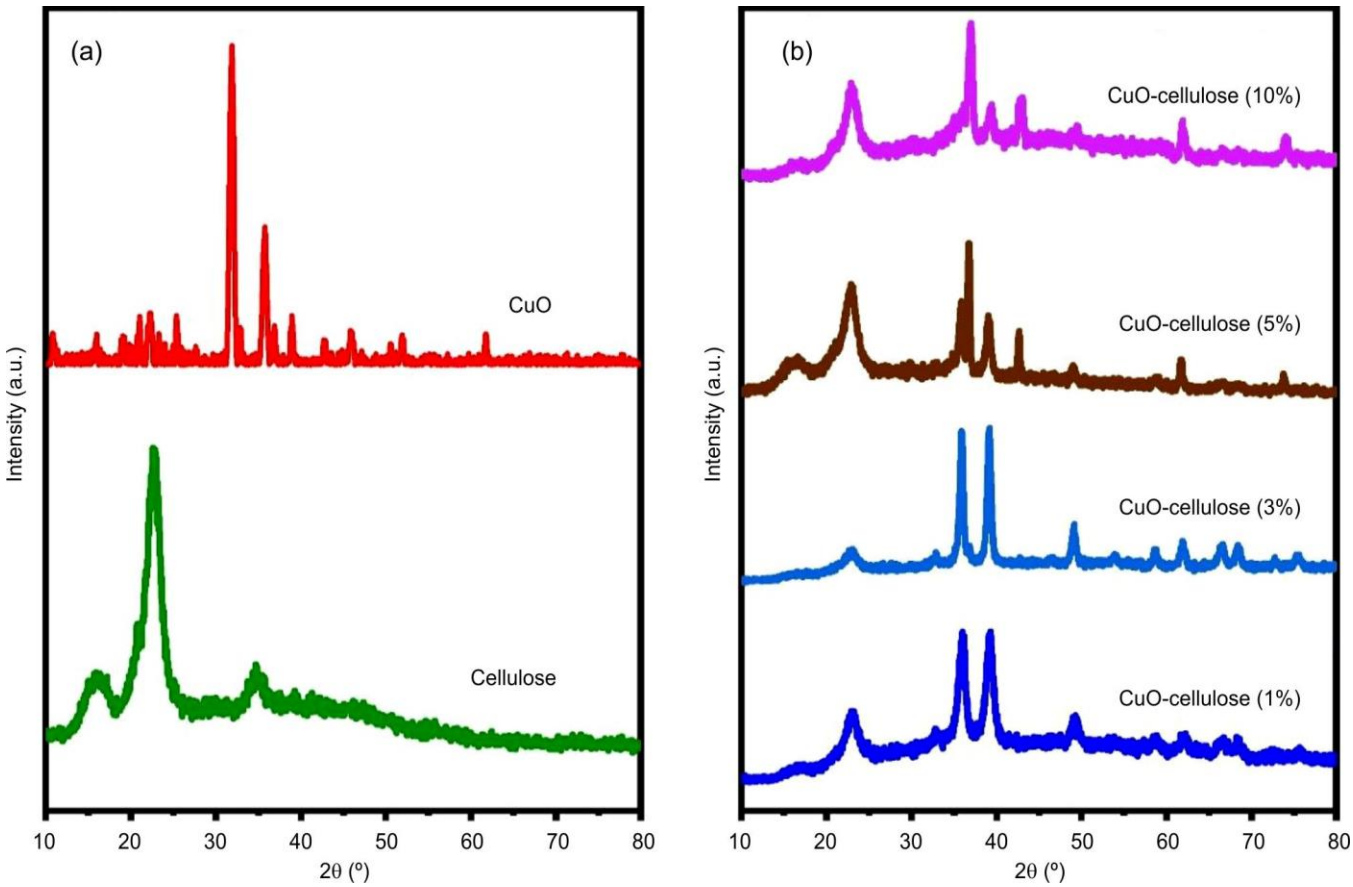

Fig. 1. XRD patterns of (a) nanostructured copper(II) oxide, (b) cellulose derived from banana peel, the pattern of copper(II) oxide-cellulose nanocomposites

along with crystalline domains. The prominent peaks at 2θ 16.40º, 22.70º and 34.45º are assigned to the (101), (002) and (040) planes of cellulose respectively, which is matched with the JCPDS card no. 00-050-0926 [49].

Fig. 1b presents the XRD patterns of various copper(II) oxide-cellulose nanocomposites with different cellulose contents *viz.* 1%, 3%, 5% and 10%. Across all nanocomposites, the characteristic diffraction peaks of both CuO and cellulose are retained, confirming the coexistence of both phases within the composites. The presence of CuO peaks at similar 2θ positions as in pure CuO suggests that the crystalline structure of CuO remains intact after incorporation into the cellulose matrix. Meanwhile, the cellulose peaks remain visible but show slight variations in intensity and peak shape, which could be attributed to interactions between CuO nanoparticles and the cellulose matrix as well as possible changes in crystallinity induced by the composite formation.

Furthermore, the diffraction peaks in the nanocomposite patterns exhibit narrow full width at half maximum (FWHM) values, indicating good crystallinity for both CuO and cellulose phases. As the cellulose content increases from 1% to 5%, the intensity of the cellulose-related peaks becomes more pronounced, reflecting the higher proportion of cellulose in the composite. Meanwhile, the characteristic CuO peaks remain consistent in position and intensity, confirming that the CuO crystalline structure is preserved and not significantly altered by the varying cellulose content. This suggests a stable integration of CuO within the cellulose matrix, where increasing cellulose concentration enhances the polymer phase without disrupting the crystalline nature of CuO. Overall, the XRD analysis clearly demonstrates the formation of CuO-cellulose nanocomposites where both constituents maintain their characteristic crystalline structures, supporting the successful synthesis of these composite materials.

FTIR analysis: The FTIR spectrum of cellulose (Fig. 2a) exhibits a broad band near 3400 cm^{-1}, attributed to O–H stretching vibrations, indicating strong hydrogen bonding interactions within the cellulose structure. The peak near 2900 cm^{-1} corresponds to the stretching vibrations of aliphatic C–H bonds, while the band at 650 cm^{-1} is assigned to O–H bending of the adsorbed water molecules. Glycosidic linkages in cellulose are confirmed by C-O-C stretching vibrations in the 1200-1000 cm^{-1} region, and deformation vibrations are observed around 1400 cm^{-1} [50]. The absence of peaks corresponding to metal oxides confirms the purity of the cellulose.

Upon incorporation of CuONPs into the cellulose matrix, additional peaks corresponding to M–O vibrations appear. The FTIR spectrum of the CuO–cellulose nanocomposite (Fig. 2b) shows a broad band around 3400 cm^{-1}, corresponding to O-H stretching vibrations from both cellulose and adsorbed water. Aliphatic C–H stretching vibrations are confirmed by the peak near 2900 cm^{-1}, while a band at 1650 cm^{-1} indicates O-H bending of adsorbed water. Cu–O stretching vibrations are observed in the 600-500 cm^{-1} range, confirming the formation

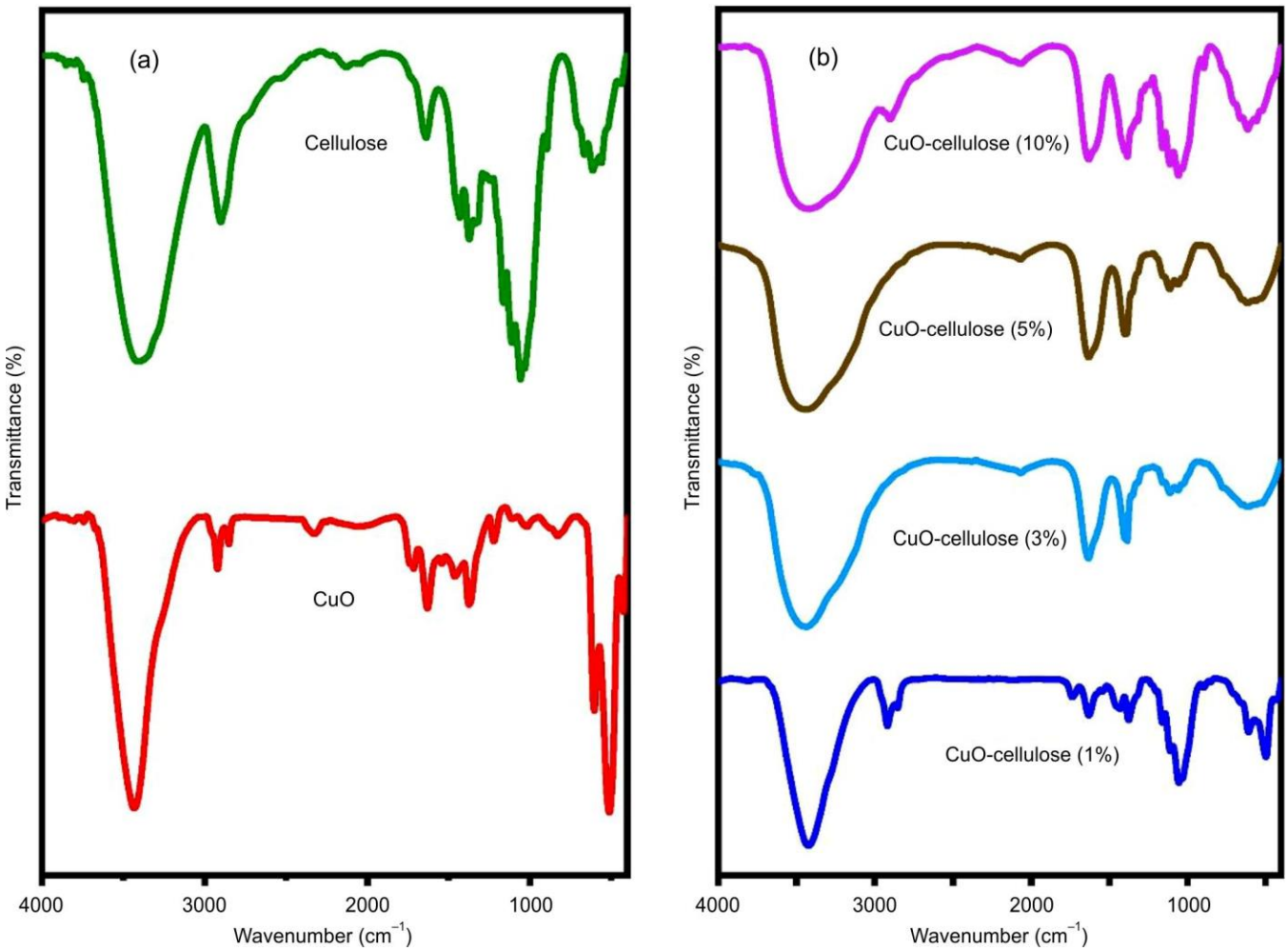

Fig. 2. Spectrum of FT-IR measurement (a) nanostructure of copper(II) oxide and extracted cellulose (b) IR spectra of copper(II) oxide-cellulose nanocomposites

of copper oxide. The absence of significant absorption in the 1000-300 cm^{-1} region reflects the inorganic nature of CuO. These spectral features confirm the successful incorporation of CuO into the cellulose matrix and the formation of the CuO–cellulose nanocomposite (3%) [51].

XPS analysis: The XPS survey spectrum of the CuO–cellulose nanocomposite (Fig. 3a) confirms the presence of carbon, oxygen, and copper, in agreement with EDX results. The high-resolution C 1s spectrum (Fig. 3b) shows multiple chemical states, for example, the peak at 284.6 eV corresponds to the C–C/C–H bonds in the cellulose backbone, 285.8 eV is attributed to C–O bonds (hydroxyl groups), 287.0 eV represents carbonyl (C=O) groups and 288.5-289.0 eV is assigned to carboxyl or ester groups (O–C=O) [52-54]. Similarly, The O 1s XPS spectrum (Fig. 3c) displays multiple peaks, indicating the presence of different oxygen species in the CuO-cellulose nanocomposites. The main peak at higher binding energy corresponds to lattice oxygen in CuO, while the smaller peaks at lower binding energies are attributed to oxygen in hydroxyl groups and adsorbed water or oxygen-containing functional groups from cellulose. This confirms the coexistence of oxygen environments related to both CuO and cellulose. The Cu 2p spectrum (Fig. 3d) exhibits peaks at 932.5 eV (Cu $2p_{3/2}$) and 952.4 eV (Cu $2p_{1/2}$), along with satellite peaks at ~941-945 eV and ~961-965 eV, confirming the presence of Cu^{2+} and ruling out Cu^{+} or metallic Cu. The dominance of the Cu^{2+} state is crucial for the photocatalytic degradation, as it facilitates efficient charge separation and reactive oxygen species (ROS) generation under visible light irradiation.

Morphology studies: SEM analysis of cellulose nanocrystals (CNCs) extracted from banana peels (Fig. 4a) shows rod-like and fibrillar structures, typical of plant-derived CNCs. The long, uneven fibers indicate successful removal of amorphous regions while preserving crystallinity. Observed agglomeration and surface roughness arise from hydrogen bonding or residual lignin. The porous morphology enhances applicability in biodegradable composites, water purification and nanocomposite reinforcement. The SEM image of CuONPs (Fig. 4b) reveal crystalline, densely packed needle-like and flaky structures with rough and porous surfaces, which increase surface area and enhance photocatalytic and adsorption properties. The uniform, hierarchical growth confirms successful synthesis.

The CuO-cellulose (3%) nanocomposite (Fig. 4c) shows the irregular shaped CuO particles dispersed on the cellulose matrix. Rod-like and fragmented structures on the fiber surface

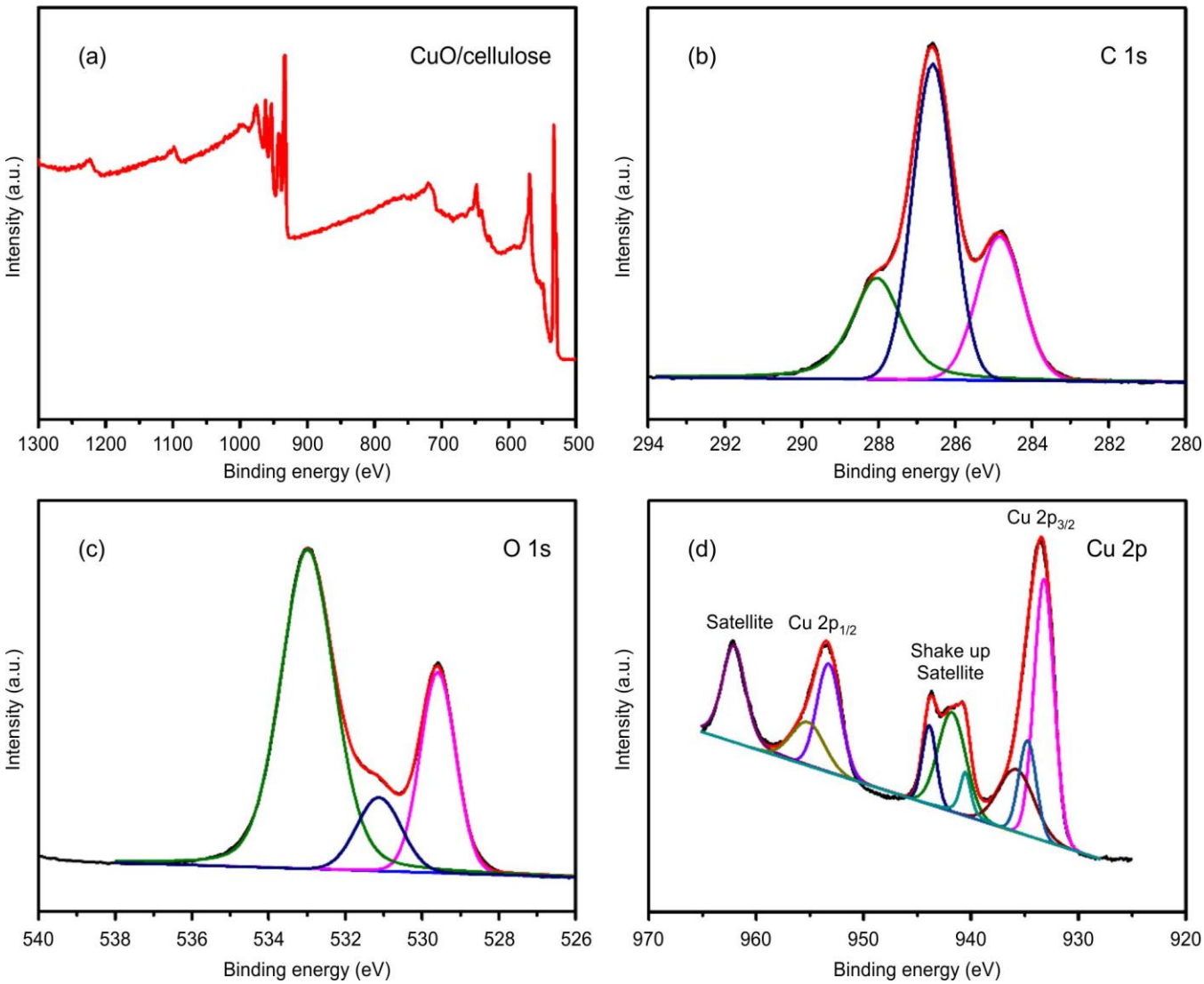

Fig. 3. XPS study of copper(II) oxide-cellulose nanocomposite represents all elements (a) copper(II) oxide-cellulose, (b) C 1s scan spectra, (c) O 1s scan spectra and (d) Cu 2p scan spectra

confirm CuO deposition, while localized agglomeration indicates strong nanoscale interactions between CuONPs and cellulose. The high porosity and rough surface of the prepared nanocomposite improve the pollutant adsorption. In this SEM image, darker regions represent the cellulose matrix, while the brighter regions correspond to CuO nanoparticles due to higher atomic number electron scattering.

The EDX analysis (Fig. 4d) confirms the presence of C (44.4 wt.%, 58.6 at.%), O (37.2 wt.%, 36.8 at.%) and Cu (18.4 wt.%, 4.6 at.%), verifying the uniform incorporation of CuONPs into the cellulose matrix. The high C and O content indicates the organic nature of cellulose, while the low Cu concentration suggests homogeneous distribution, which enhances surface contact and photocatalytic efficiency.

DRS measurement: Fig. 5a-b shows the UV-Vis DRS and Tauc's plots of CuONPs and copper(II) oxide-cellulose nanocomposites with varying cellulose contents (1-10%), respectively. Using the Kubelka-Munk function, the optical band gaps were determined, indicating enhanced visible-light absorption with cellulose copper(II) oxide loading.

$$(\alpha h\nu)^{1/n} = A(h\nu - E_g) \quad (1)$$

where the absorption coefficient (α), photon frequency (ν) and Planck's constant (h) are used in the Tauc equation to find out the optical energy bandgap (E_g), the nature of optical transitions. The constant (A) is used to represent the difference in the electronic structure, which varies with the types of material. This allowed transition was n = 2 and n = 1/2 at indirect [46]. It has been found that CuO-cellulose nanocomposite is fully capable of enhancing the interfacial electronic transition, which increases the ability of photocatalysis.

Photocatalytic studies: The synthesized copper(II) oxide-cellulose nanocomposites immobilized in aqueous thymol blue (ThB) solution showed the efficient dye removal by means of photocatalytic degradation ability in the presence of visible light irradiation. The absorption and dissolution behaviour of thymol blue (ThB) was evaluated by monitoring its concentration at predetermined time intervals using a UV-Vis spectrophotometer (Shimadzu, Japan). Photodegradation experiments

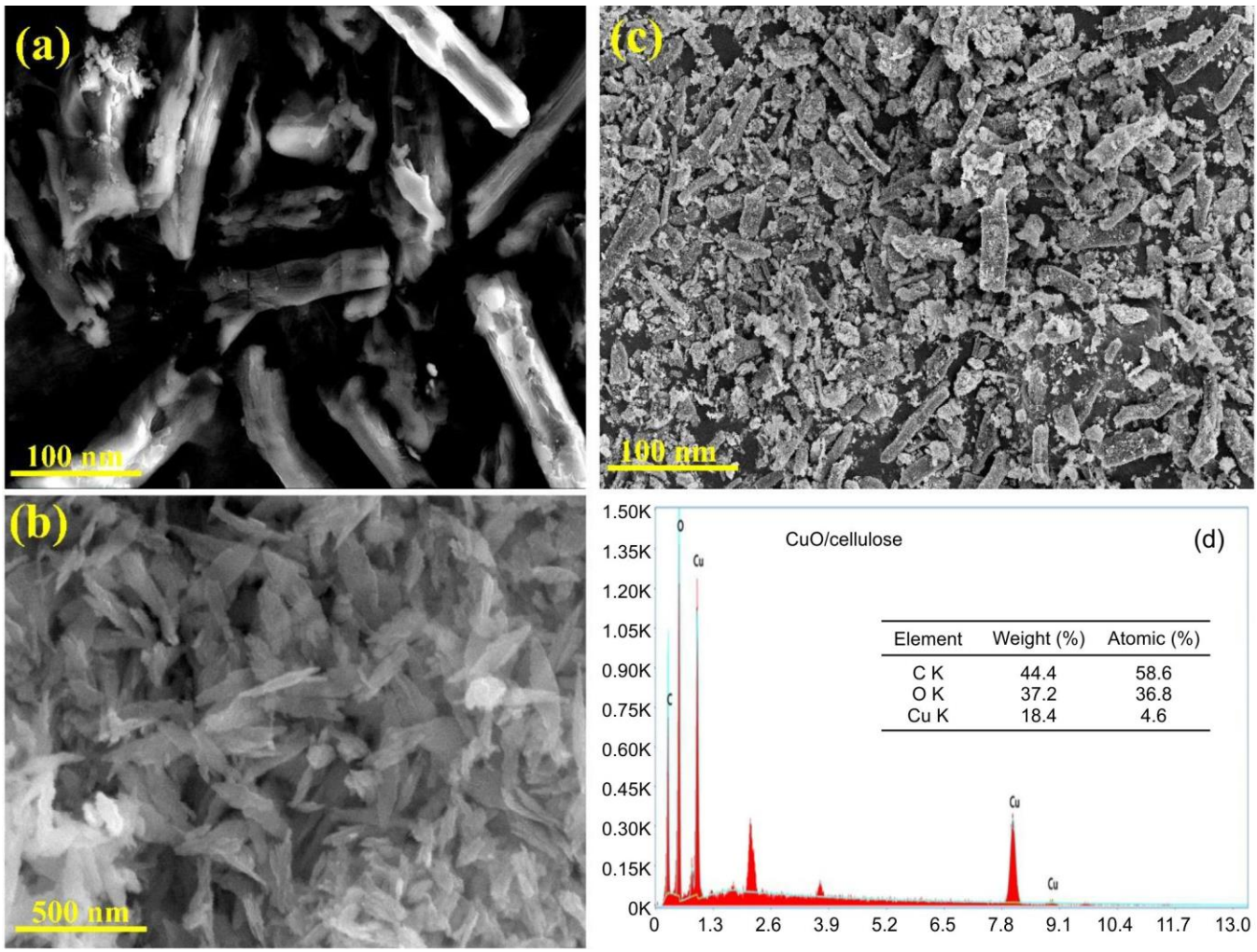

Fig. 4. FE-SEM images: (a) extracted cellulose, (b) nanostructured copper(II) oxide, (c) copper(II) oxide-cellulose nanocomposite and (d) EDX spectra for elemental composition of copper(II) oxide-cellulose nanocomposite

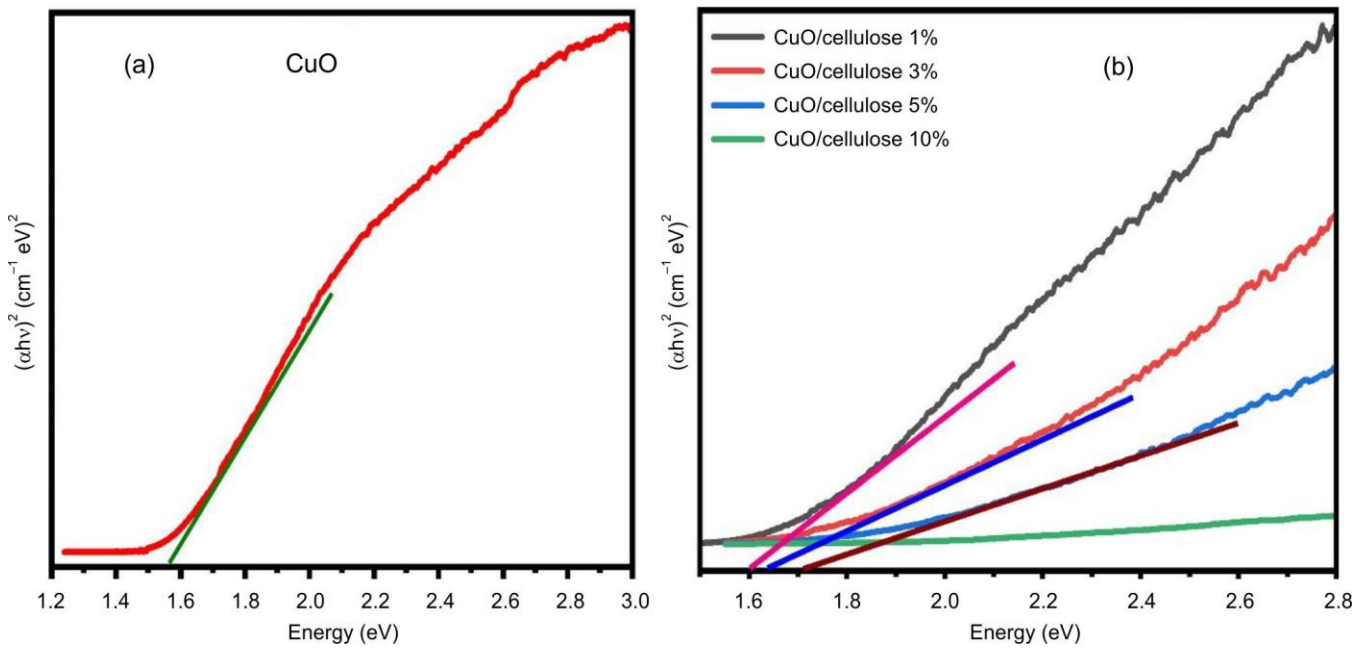

Fig. 5. DRS plot: (a) copper nanoparticles and (b) copper(II) oxide-cellulose nanocomposites band gap by Tauc's plot

were carried out under controlled conditions at pH 7.0 and 28 ºC. The study systematically examined the effects of catalyst dosage, cellulose content, reaction time, visible-light intensity and varying CuO-to-cellulose ratios on the photocatalytic performance.

The incorporation of cellulose into the CuO-cellulose nanocomposites markedly modifies their optical characteristics by lowering the band-gap energy and enhancing photon absorption. The functional groups present in cellulose (epoxy, carboxyl and hydroxyl), combined with π-π interactions within the polymeric structure, promote efficient charge separation and increase carrier mobility. This synergistic behaviour improves adsorption capacity while effectively suppressing electron–hole recombination, thereby significantly boosting the photocatalytic activity of the nanocomposites [55,56].

The adsorption behaviour of ThB prior to visible-light irradiation was assessed using the copper(II) oxide-cellulose nanocomposites, as illustrated in Fig. 6. After the adsorption stage, the solutions were exposed to visible light using various nanocomposite formulations. The photocatalytic degradation efficiency was subsequently calculated using eqn. 2 [57]:

$$\text{Efficiency (\%)} = \frac{C_o - C_t}{C_o} \times 100 \qquad (2)$$

where C_o and C_t are the ThB concentrations at t = 0 and t = t, respectively.

Fig. 7a-b illustrates the photocatalytic activity of the prepared CuO-cellulose nanocomposites containing 1, 3, 5 and 10% cellulose under visible-light irradiation at different catalyst dosages. The influence of CuO content on photocatalytic efficiency is clearly evident. The experimental results show that all CuO-cellulose nanocomposites exhibit significantly enhanced degradation of ThB compared to pure CuO. This improvement is attributed to the presence of cellulose, which suppresses electron–hole recombination and facilitates the generation of reactive oxygen species (ROS), thereby markedly improving photocatalytic performance [55].

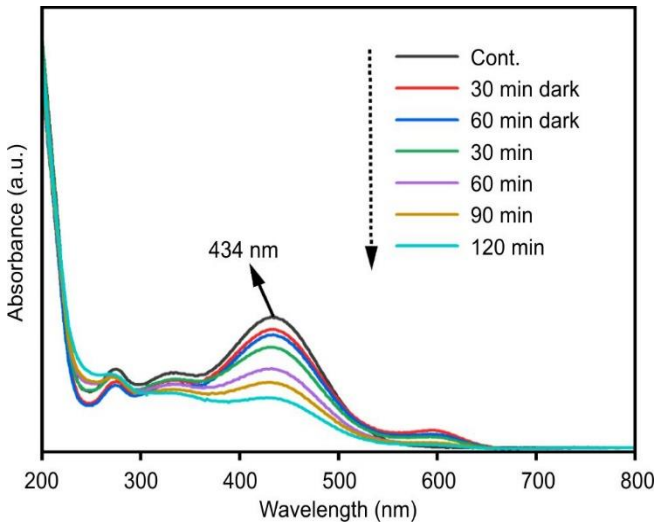

Fig. 6. Photodegradation plot of ThB

Photodegradation studies of ThB under visible-light exposure revealed that the CuO-cellulose-3% nanocomposite at a dosage of 0.20 g/L demonstrated the highest degradation efficiency among all tested formulations. Additional experiments using different concentrations of the CuO-cellulose-3% sample (0.10, 0.20, 0.30 and 0.40 g/L) were performed to evaluate dosage-dependent effects. As shown in Fig. 7b, the 0.20 g/L dosage exhibited the most efficient photocatalytic degradation of ThB. The optimal cellulose content enhances interfacial electron transfer between cellulose and CuO, improves optical absorption and surface activity, and promotes the formation of ROS responsible for efficient degradation and mineralization of ThB into less toxic byproducts.

A comparative summary in Table-1 demonstrates that the photocatalytic efficiency achieved in this study surpasses previously reported results, primarily due to the improved composition, optimized cellulose incorporation, and superior optical properties of the CuO-cellulose nanocomposites.

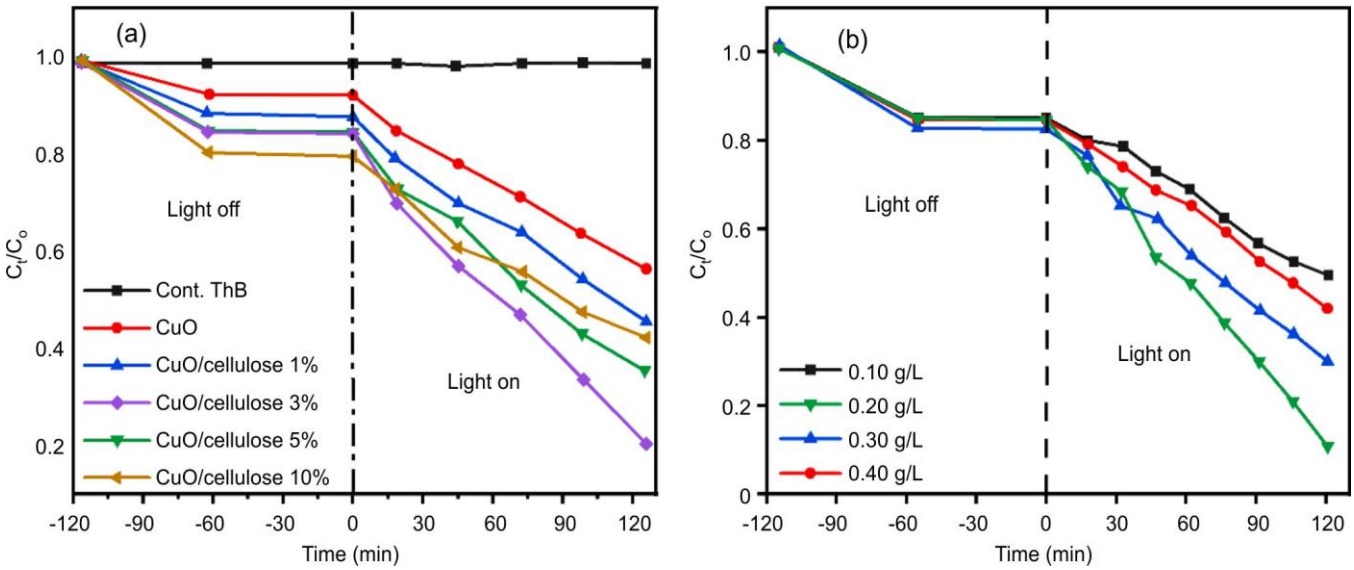

Fig. 7. Photodegradation plot of ThB dye (a) C_t/C_o *vs.* interaction time for various copper(II) oxide-cellulose nanocomposites (b) C_t/C_o *vs.* interaction time for different dosage (0.20 g/L) of copper(II) oxide-cellulose nanocomposites

TABLE-1
COMPARISON DATA OF PHOTOCATALYTIC PERFORMANCE OF REPORTED DIFFERENT NANOCOMPOSITES FOR THYMOL BLUE (ThB) DEGRADATION

Photocatalyst	Pollutant (dye) (mg/L)	Light source	Degradation time (min)	Degradation (%)	Ref.
Titania-alumina-zinc-ferrite NCs	ThB (50 mg/L)	UV light (8 W mercury lamp)	900	90	[58]
ZnO-Al_2O_3 NCs	ThB (200 mg/L)	Solar light	240	97	[42]
($CuMoO_4$)-doped bismuth titanate alloy	ThB	UV light	240	50	[59]
TiO_2/PANI/GO nanocomposite	ThB (25 mg/L)	UV (450 W Hanovia lamp)	180	96	[60]
CuO-cellulose nanocomposite	ThB (20 mg/L)	Visible light	120	98	Present work

Mechanism: The photodegradation of ThB molecules under visible-light irradiation using CuO-cellulose nanocomposites proceeds through a sequence of photocatalytic reactions, as illustrated in Fig. 8. The cellulose matrix supports and stabilizes the photoactive CuONPs, thereby enhancing their catalytic performance. Upon exposure to visible light, CuONPs, an efficient semiconductor with a narrow band gap of 1.2-1.9 eV, absorbs photons, promoting electrons from the valence band (VB) to the conduction band (CB) and generating positively charged holes (h^+) in the VB.

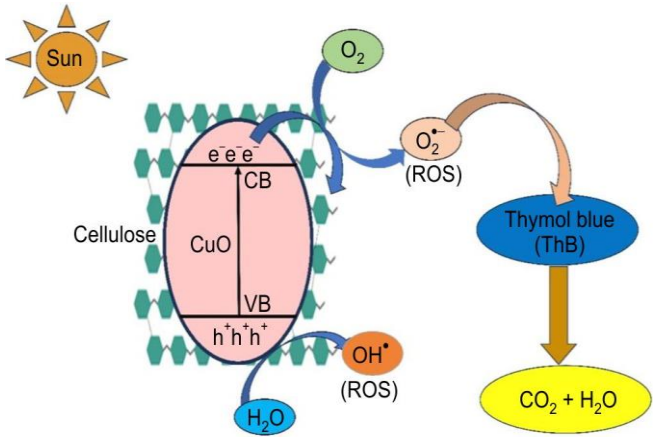

Fig. 8. Schematic illustration of photocatalytic degradation mechanism for ThB dye using copper(II) oxide-cellulose nanocomposite

Cellulose acts as an electron-transport scaffold, improving nanoparticle dispersion and suppressing the recombination of photogenerated charge carriers. The CB electrons of CuO reduce dissolved oxygen molecules (O_2), producing superoxide radicals ($O_2^{\bullet-}$). Simultaneously, the VB holes oxidize water molecules or hydroxide ions to form highly reactive hydroxyl radicals ($^\bullet$OH). These generated ROS, primarily $O_2^{\bullet-}$ and $^\bullet$OH, attack and decompose ThB molecules, ultimately converting them into environmentally benign products such as CO_2, H_2O and inorganic ions. This synergistic interaction between CuONPs and cellulose significantly enhances the photocatalytic degradation efficiency. Based on these facts, the mechanism has been proposed based on the following eqns:

$$\text{CuO/Cellulose} + h\nu \rightarrow e^-(CB) + h^+(VB) \quad (3)$$

$$e^- + O_2 \rightarrow O_2^{\bullet-} \quad (4)$$

$$h^+ + H_2O \rightarrow OH^\bullet + H + ... \quad (5)$$

$$h^+ + OH^- \rightarrow OH^\bullet \quad (6)$$

$$\text{ThB} + OH^\bullet / O_2^{\bullet-} \rightarrow \text{Degradation intermediates} \rightarrow CO_2 + H_2O \quad (7)$$

Conclusion

In this work, copper(II) oxide–cellulose nanocomposites were successfully synthesized using cellulose extracted from banana peel waste, demonstrating a sustainable and cost-effective approach to photocatalyst fabrication. The nanocomposites exhibited excellent photocatalytic performance in the degradation of thymol blue dye under visible-light irradiation. Among the different formulations, the CuO-cellulose-3% nanocomposite achieved the highest degradation efficiency (98%), highlighting the critical role of optimized CuO loading. The structural, morphological and optical characterization confirmed the effective incorporation of CuONPs into the cellulose matrix and revealed enhanced properties that promote efficient charge separation, improved electron transport and reduced charge recombination. The remarkable photocatalytic activity is attributed to the synergistic interaction between the semiconductor CuONPs and the cellulose support. Overall, the results demonstrate that cellulose derived from agricultural waste can be effectively combined with metal oxide nanoparticles to produce a highly efficient, eco-friendly and sustainable photocatalyst for wastewater treatment applications.

ACKNOWLEDGEMENTS

The authors are thankful to Department of Chemistry, Gurukul Kangri (Deemed to be University), Haridwar, India, for providing better laboratory facilities. One of the authors, Hafeezur Rehmaan acknowledge to University Grant Commission (UGC), Government of India (G.O.I.) for providing the Junior Research fellowship (JRF) (file. No. 16-6(DEC.2018)/2019(NET/CSIR) and our heartfelt appreciation goes to IIT Roorkee and NIT Jaipur for providing instrumental facilities.

CONFLICT OF INTEREST

The authors declare that there is no conflict of interests regarding the publication of this article.

DECLARATION OF AI-ASSISTED TECHNOLOGIES

During the preparation of this manuscript, the authors used an AI-assisted tool(s) to improve the language. The authors reviewed and edited the content and take full responsibility for the published work.

REFERENCES

1. O.O. Alegbeleye and A.S. Sant'Ana, *Int. J. Hyg. Environ. Health*, **227**, 113524 (2020); https://doi.org/10.1016/j.ijheh.2020.113524
2. C. Hu, X. Yan, W. Gong, X. Liu, L. Wang and L. Gao, *Swarm Evol. Comput.*, **55**, 100674 (2020); https://doi.org/10.1016/j.swevo.2020.100674
3. Q.L. Chen and H.L. Chen, *J. Nanopart. Res.*, **26**, 189 (2024); https://doi.org/10.1007/s11051-024-06105-0
4. J. Gao, H. Jang, L. Huang and K.R. Matthews, *Int. J. Food Microbiol.*, **323**, 108593 (2020); https://doi.org/10.1016/j.ijfoodmicro.2020.108593
5. B. Prandi, A. Faccini, F. Lambertini, M. Bencivenni, M. Jorba, B. Van Droogenbroek, G. Bruggeman, J. Schöber, J. Petrusan, K. Elst and S. Sforza, *Food Chem.*, **286**, 567 (2019); https://doi.org/10.1016/j.foodchem.2019.01.166
6. V.K. Gaur, P. Sharma, R. Sirohi, M.K. Awasthi, C.G. Dussap and A. Pandey, *J. Hazard. Mater.*, **398**, 123019 (2020); https://doi.org/10.1016/j.jhazmat.2020.123019
7. N. Tavker and M. Sharma, *J. Environ. Manage.*, **255**, 109906 (2020); https://doi.org/10.1016/j.jenvman.2019.109906
8. X. Zheng, W. Chen, M. Xu, C. Cai and F. Yang, *J. Nanopart. Res.*, **25**, 96 (2023); https://doi.org/10.1007/s11051-023-05748-9
9. J. Duraimurugan, *Optik*, **202**, (2020); https://doi.org/10.1016/j.ijleo.2019.163607
10. M. Maruthupandy, P. Qin, T. Muneeswaran, G. Rajivgandhi, F. Quero and J.M. Song, *Mater. Sci. Eng. B*, **254**, 114516 (2020); https://doi.org/10.1016/j.mseb.2020.114516
11. M. Kadhom, N. Albayati, H. Alalwan and M. Al-Furaiji, *Sustain. Chem. Pharm.*, **16**, 100259 (2020); https://doi.org/10.1016/j.scp.2020.100259
12. H. Soni, N. Kumar, K. Patel and R.N. Kumar, *Desalination Water Treat.*, **57**, 19857 (2016); https://doi.org/10.1080/19443994.2015.1102091
13. K. Rokesh, S.C. Mohan, S. Karuppuchamy and K. Jothivenkatachalam, *J. Environ. Chem. Eng.*, **6**, 3610 (2018); https://doi.org/10.1016/j.jece.2017.01.023
14. M. Hasanpour and M. Hatami, *J. Mol. Liq.*, **309**, 113094 (2020); https://doi.org/10.1016/j.molliq.2020.113094
15. O. Mekasuwandumrong, P. Pawinrat, P. Praserthdam and J. Panpranot, *Chem. Eng. J.*, **164**, 77 (2010); https://doi.org/10.1016/j.cej.2010.08.027
16. L. Abramian and H. El-Rassy, *Chem. Eng. J.*, **150**, 403 (2009); https://doi.org/10.1016/j.cej.2009.01.019
17. I. Ali and V.K. Gupta, *Nat. Protoc.*, **1**, 2661 (2006); https://doi.org/10.1038/nprot.2006.370
18. G.K. Upadhyay, J.K. Rajput, T.K. Pathak, P.K. Pal and L.P. Purohit, *Appl. Surf. Sci.*, **509**, 145326 (2020); https://doi.org/10.1016/j.apsusc.2020.145326
19. C.A. Jaramillo-Páez, J.A. Navío, M.C. Hidalgo and M. Macías, *Catal. Today*, **313**, 12 (2018); https://doi.org/10.1016/j.cattod.2017.12.009
20. P. Dumrongrojthanath, T. Thongtem, A. Phuruangrat and S. Thongtem, *Superlattices Microstruct.*, **64**, 196 (2013); https://doi.org/10.1016/j.spmi.2013.09.028
21. A. Phuruangrat, A. Maneechote, P. Dumrongrojthanath, N. Ekthammathat, S. Thongtem and T. Thongtem, *Superlattices Microstruct.*, **78**, 106 (2015); https://doi.org/10.1016/j.spmi.2014.11.038
22. S.S.P. Selvin, N. Radhika, O. Borang, S. Lydia and J.P. Merlin, *J. Mater. Sci. Mater. Electron.*, **28**, 6722 (2017); https://doi.org/10.1007/s10854-017-6367-y
23. R. Saleh and N.F. Djaja, *Spectrochim. Acta A Mol. Biomol. Spectrosc.*, **130**, 581 (2014); https://doi.org/10.1016/j.saa.2014.03.089
24. M. Shkir, B.M. Al-Shehri, M.P. Pachamuthu, A. Khan, K.V. Chandekar, S. AlFaify and M.S. Hamdy, *Colloids Surf. A Physicochem. Eng. Asp.*, **587**, 124340 (2020); https://doi.org/10.1016/j.colsurfa.2019.124340
25. Z. Sun, L. Shi, Y. Li, L. Liu, Z. Liu, Z. Yin and X. Qu, *J. Nanopart. Res.*, **24**, 220 (2022); https://doi.org/10.1007/s11051-022-05599-w
26. R. Bedoić, A. Špehar, J. Puljko, L. Čuček, B. Ćosić, T. Pukšec and N. Duić, *Renew. Sustain. Energy Rev.*, **130**, 109951 (2020); https://doi.org/10.1016/j.rser.2020.109951
27. S. Baturay, A. Tombak, D. Kaya, Y.S. Ocak, M. Tokus, M. Aydemir and T. Kilicoglu, *J. Sol-Gel Sci. Technol.*, **78**, 422 (2016); https://doi.org/10.1007/s10971-015-3953-4
28. A. Wongrakpanich, I.A. Mudunkotuwa, S.M. Geary, A.S. Morris, K.A. Mapuskar, D.R. Spitz, V.H. Grassian and A.K. Salem, *Environ. Sci. Nano*, **3**, 365 (2016); https://doi.org/10.1039/C5EN00271K
29. H.W. Wu, S.Y. Lee, W.C. Lu and K.S. Chang, *Appl. Surf. Sci.*, **344**, 236 (2015); https://doi.org/10.1016/j.apsusc.2015.03.122.
30. S.H. Kim, A. Umar and S.W. Hwang, *Ceram. Int.*, **41**, 9468 (2015); https://doi.org/10.1016/j.ceramint.2015.04.003
31. T. Baran, A. Visibile, M. Busch, X. He, S. Wojtyla, S. Rondinini, A. Minguzzi and A. Vertova, *Molecules*, **26**, 7271 (2021); https://doi.org/10.3390/molecules26237271
32. A.M. Ibrahim, A.R. Galaly, M.Sh. Abdel-Wahab, M. Shaban, W.Z. Tawfik and M.T. Tammama, *RSC Adv.*, **15**, 24612 (2025); https://doi.org/10.1039/D5RA04234H
33. S.V. Gupta, V.V. Kulkarni and M. Ahmaruzzaman, *Sci. Rep.*, **13**, 3009 (2023); https://doi.org/10.1038/s41598-023-30096-y
34. X. Zhang, G. Wang, X. Liu, J. Wu, M. Li, J. Gu, H. Liu and B. Fang, *J. Phys. Chem. C*, **112**, 16845 (2008); https://doi.org/10.1021/jp806985k
35. M. Vaseem, A. Umar, Y.B. Hahn, D.H. Kim, K.S. Lee, J.S. Jang and J.S. Lee, *Catal. Commun.*, **10**, 11 (2008); https://doi.org/10.1016/j.catcom.2008.07.022
36. Q. Zhang, K. Zhang, D. Xu, G. Yang, H. Huang, F. Nie, C. Liu and S. Yang, *Prog. Mater. Sci.*, **60**, 208 (2014); https://doi.org/10.1016/j.pmatsci.2013.09.003
37. A. Alam, A. Hassan, Z. Sultana and N. Das, *RSC Sustain.*, **3**, 5027 (2025); https://doi.org/10.1039/D5SU00369E
38. Y. Yang, X. Li, C. Wan, Z. Zhang, W. Cao, G. Wang and Y. Wu, *Collagen & Leather*, **6**, 35 (2024); https://doi.org/10.1186/s42825-024-00179-1
39. J.H. Kim, B.S. Shim, H.S. Kim, Y.J. Lee, S.K. Min, D. Jang, Z. Abas and J. Kim, *Int. J. Precis. Eng. Manuf. Green Technol.*, **2**, 197 (2015); https://doi.org/10.1007/s40684-015-0024-9
40. C. Katepetch, R. Rujiravanit and H. Tamura, *Cellulose*, **20**, 1275 (2013); https://doi.org/10.1007/s10570-013-9892-8
41. Y. Kuang, X. Zhang and S. Zhou, *Water*, **12**, 587 (2020); https://doi.org/10.3390/w12020587
42. S. Sowrirajan, G. Maheshwari and B. Joseph, *Mater. Today Proc.*, **55**, 226 (2022); https://doi.org/10.1016/j.matpr.2021.06.342
43. G. Manjari, S. Saran, T. Arun, A. Vijaya Bhaskara Rao and S.P. Devipriya, *J. Saudi Chem. Soc.*, **21**, 610 (2017); https://doi.org/10.1016/j.jscs.2017.02.004
44. H.A. Al-Aoh, I.A.M. Mihaina, M.A. Alsharif, A.A.A. Darwish, M. Rashad, S.K. Mustafa, M.M.H. Aljohani, M.A. Al-Duais and H.S. Al-Shehri, *Chem. Eng. Commun.*, **207**, 1719 (2020); https://doi.org/10.1080/00986445.2019.1680366
45. V. Srivastava and A.K. Choubey, *J. Mol. Struct.*, **1242**, 130749 (2021); https://doi.org/10.1016/j.molstruc.2021.130749
46. T. Munawar, S. Yasmeen, F. Hussain, K. Mahmood, A. Hussain, M. Asghar and F. Iqbal, *Mater. Chem. Phys.*, **249**, 122983 (2020); https://doi.org/10.1016/j.matchemphys.2020.122983
47. S. Kumar, R.D. Kaushik and L.P. Purohit, *J. Colloid Interface Sci.*, **632**, 196 (2023); https://doi.org/10.1016/j.jcis.2022.11.040
48. P. Mallick, *Proc. Natl. Acad. Sci., India, Sect. A Phys. Sci.*, **84**, 387 (2014); https://doi.org/10.1007/s40010-014-0131-y
49. R.K. Hussain, W.J. Aziz and I.A. Ibrahim, *J. Nanostruct.*, **9**, 761 (2019); https://doi.org/10.22052/JNS.2019.04.017
50. V. Bisla, G. Rattan, S. Singhal and A. Kaushik, *Int. J. Biol. Macromol.*, **161**, 194 (2020); https://doi.org/10.1016/j.ijbiomac.2020.06.035

51. I.M.S. Araújo, R.R. Silva, G. Pacheco, W.R. Lustri, A. Tercjak, J. Gutierrez, J.R.S. Júnior, F.H.C. Azevedo, G.S. Figuêredo, M.L. Vega, S.J.L. Ribeiro and H.S. Barud, *Carbohydr. Polym.*, **179**, 341 (2018); https://doi.org/10.1016/j.carbpol.2017.09.081
52. P. Sagar, M. Srivastava and S.K. Srivastava, *ChemistrySelect*, **7**, 202202271 (2022); https://doi.org/10.1002/slct.202202271
53. S. Kumaraguru, S. Raghu, R. Subadevi, M. Sivakumar and R. Gnanamuthu, *Ionics*, **27**, 5043 (2021); https://doi.org/10.1007/s11581-021-04155-1
54. S. Kumaraguru, S. Raghu, P. Rajkumar, R. Subadevi, M. Sivakumar, C.W. Lee and R.M. Gnanamuthu, *Ionics*, **27**, 1049 (2021); https://doi.org/10.1007/s11581-021-03901-9
55. M. Khandelwal, K. Soni, K.P. Misra, A. Bagaria, D.S. Rathore, G. Pemawat, R. Singh and R.K. Khangarot, *RSC Adv.*, **15**, 3365 (2025); https://doi.org/10.1039/D4RA08437C
56. A.L.T. Zheng, S. Sabidi, M.A. Maran, K.B. Tan, K. Wong, E.L.T. Chung and Y. Andom, *BioResources*, **20**, 9148 (2025); https://doi.org/10.15376/biores.20.4.9148-9166
57. A.S. Elfeky, S.S. Salem, A.S. Elzaref, M.E. Owda, H.A. Eladawy, A.M. Saeed, M.A. Awad, R.E. Abou-Zeid and A. Fouda, *Carbohydr. Polym.*, **230**, 115711 (2020); https://doi.org/10.1016/j.carbpol.2019.115711
58. P.P. Hankare, R.P. Patil, A.V. Jadhav, K.M. Garadkar and R. Sasikala, *Appl. Catal. B*, **107**, 333 (2011); https://doi.org/10.1016/j.apcatb.2011.07.033
59. T.K. Ghorai, D. Dhak, S. Dalai and P. Pramanik, *Mater. Res. Bull.*, **43**, 1770 (2008); https://doi.org/10.1016/j.materresbull.2007.07.009
60. A. Kumar, C.J. Raorane, A. Syed, A.H. Bahkali, A.M. Elgorban, V. Raj and S.C. Kim, *Environ. Res.*, **216**, 114741 (2023); https://doi.org/10.1016/j.envres.2022.114741